Detecting dark-matter waves with a network of precision-measurement tools

Andrei Derevianko

Department of Physics, University of Nevada, Reno, Nevada 89557, USA

Virialized ultralight fields (VULFs) are viable cold dark-matter candidates and include scalar and pseudoscalar bosonic fields, such as axions and dilatons. Direct searches for VULFs rely on low-energy precision-measurement tools. While previous proposals have focused on detecting coherent oscillations of the VULF signals at the VULF Compton frequencies for individual devices, here I consider a network of such devices. Virialized ultralight fields are essentially dark-matter waves and as such they carry both temporal and spatial phase information. Thereby, the discovery reach can be improved by using networks of precision-measurement tools. To formalize this idea, I derive a spatiotemporal two-point correlation function for the ultralight dark-matter fields in the framework of the standard halo model. Due to VULFs being Gaussian random fields, the derived two-point correlation function fully determines N-point correlation functions. For a network of N_D devices within the coherence length of the field, the sensitivity compared to a single device can be improved by a factor of $\sqrt{N_D}$. Further, I derive a VULF dark-matter signal profile for an individual device. The resulting line shape is strongly asymmetric due to the parabolic dispersion relation for massive nonrelativistic bosons. I discuss the aliasing effect that extends the discovery reach to VULF frequencies higher than the experimental sampling rate. I present sensitivity estimates and develop a stochastic field signal-to-noise ratio statistic. Finally, I consider an application of the formalism developed to atomic clocks and their networks.

I. INTRODUCTION

Exacting the microscopic nature of dark matter (DM) is one of grand challenges of modern physics and cosmology [1,2]. Here I focus on a general class of DM candidates: ultralight bosonic fields. These include both pseudoscalar and scalar fields, axions being the example of pseudoscalars and dilatons of the scalars. I will collectively refer to such ultralight fields as virialized ultralight fields (VULFs). Such fields behave as classical entities coherent on a scale of individual devices and can be searched for with low-energy precision-measurement tools. Precision measurements, with their exquisite precision, have been historically important [3] in powerfully constraining new physics beyond the standard model (SM) and can be repurposed for dark-matter searches.

Individual direct VULF DM search proposals cover a broad range of experiments [4–11], e.g., atomic clocks, magnetometers, accelerometers, interferometers, cavities, resonators, and permanent electric dipole and parity-violation measurements, and extend to gravitational wave detectors. The sought DM signature in these proposals is DM-induced oscillations of the measured signals at the VULF Compton frequencies at the device location. All these proposals can either discover VULFs or substantially constrain yet unexplored parameter space. These distinct tools can be located at geographically separated laboratories across several continents or in space and one can envision a network of such tools as a global DM observatory. The network can be heterogenous, i.e., nodes can be populated with different kinds of devices. Here I explore the DM-induced temporal and spatial correlations between nodes of such a global network with the goal of analyzing the network's discovery potential.

An important point is that VULFs are *waves*, and while they do induce an oscillating in time signal at a given spatial location, DM signals at different locations have a fixed phase relation [see Fig. 1(a)], i.e., the signals are correlated. Based on this observation, here we argue that a wider discovery reach can be gained by sampling the DM wave at several locations via a network of precision-measurement tools. Further, the VULF signal is composed of interfering waves traveling at different velocities and in different directions. Then the problem of relating signals at different space-time locations requires computations of dark-matter correlation functions, derived here. Based on these ideas and derivations, one can envision a number of DM wave detection experiments. In the most basic version, the modifications to already running experiments are minor and only require simple global positioning system–assisted (GPS-assisted) time stamping of data acquisition [12]. Previously, a network of precision-measurement devices have been proposed for detecting clumpy DM objects sweeping through the networks [13,14]. Here we show that such networks can be used also as discovery tools for VULF "wavy" dark matter.

This paper also addresses the difference between the deterministic and stochastic nature of ultralight dark-matter fields as detected by an individual device. It seems that so far the previous VULF literature approach was to treat ultralight dark-matter field signals as deterministic. This is related to the long coherence times of VULFs on a timescale of a typical measurement campaign. As discussed in this paper, individual devices can also be sensitive to the VULF of frequencies much higher than the sampling rate through the aliasing effect inherent to discretized measurements. For such high-frequency fields the coherence time is reduced and the more adequate
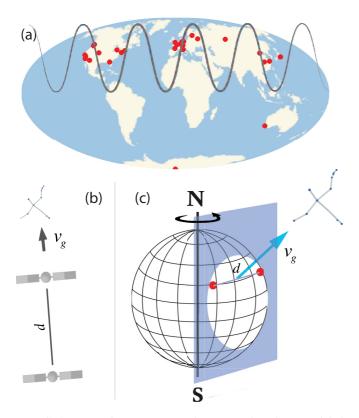
FIG. 1. (a) Dark-matter wave observatory based on a global network of existing low-energy precision-measurement laboratories (red dots) around the globe. (b) Satellite mission for probing VULF DM correlation function; both the distance between the satellites and the angle between galactic velocity $\mathbf{v}_g$ and separation $\mathbf{d}$ vectors can be varied. (c) Terrestrial experiment with fixed nodes utilizes the daily variation of the angle between the galactic velocity and two-node separation vector.

description is the stochastic approach of this paper. I derive the expected line shape of a stochastic dark-matter signal and present a frequency-space data analysis strategy. I also discuss an application of the developed formalism to atomic clocks.

This paper is organized as follows. Section II presents the derivation of the N-point correlation function for ultralight dark-matter fields. Section III explores the VULF parameter space. Section IV presents the VULF dark-matter line shape for an individual device signal. Section V extends the discussion to a network of devices. Implications of the formalism and specific data analysis strategies are discussed in Sec. VI. This section also addresses the importance of the aliasing effect in the search for high-frequency VULF DM signals and introduces SNR statistic based on the derived correlation function. An illustrative application of some of the ideas to atomic clock DM searches is presented in Sec. VII. Section VIII draws conclusions. Appendix A reviews the discrete Fourier transform and frequency-space probability distributions for deterministic and stochastic signals. Appendixes B and C present derivations of certain equations. Since the intended audience includes both atomic and particle physics communities, I restore $\hbar$ and c in the formulas in favor of using natural or atomic units. I use the rationalized Heaviside-Lorentz units for electromagnetism.

II. CORRELATION FUNCTION FOR ULTRALIGHT DARK-MATTER FIELDS

In the VULF models, dark matter is composed of ultralight spin-0 bosonic fields, oscillating at their Compton frequency $\omega_\phi = m_\phi c^2/\hbar$, where m_ϕ is the boson mass (see, e.g., the review in [15]). The frequencies can span many orders of magnitude: 10^{-10} Hz $\lesssim f_\phi = \omega_\phi/2\pi \lesssim 10^{15}$ Hz for 10^{-24} eV $\lesssim m_\phi \lesssim 10$ eV. Here the lower bound comes from requiring that the virial de Broglie wavelength is smaller than the galactic size and the upper limit from requiring that number of particles per de Broglie volume is macroscopic. I formalize these estimates below. The proposals [4–8,10] have focused on searching for an oscillating signal at the Compton frequency. Unfortunately, in a laboratory environment, an observation of an oscillating signal could be ascribed to some mundane ambient noise and it is desirable to establish additional DM signatures. To this end, in this section, I derive VULF spatiotemporal correlation functions and explore its experimental significance in later parts of the paper.

A. Linear SM-DM portals

Additional phenomenological commonality of all the VULF searches is the coupling of DM fields to SM particles and fields in terms of so-called portals, when the gauge-invariant operators of the SM fields $\mathcal{O}_X$ are coupled to the operators involving DM fields [14,16]. One of possibilities is the portal linear in the VULF field $\phi(t, \mathbf{r})$,

$$-\mathcal{L}_{\text{lin}} = \sqrt{\hbar c}\, \phi(t, \mathbf{r}) \sum_X \gamma_X \mathcal{O}_X. \tag{1}$$

Here we introduced coupling strengths γ_X; these are to be determined as a result of a positive DM signal detection or constrained otherwise. Fixing the units of fields ϕ to be that of energy ε, $[\gamma_X] = [\varepsilon]^{-1}$ and one could equivalently parametrize the linear portal (1) in terms of energy scales $\Lambda_X = 1/|\gamma_X|$.

For axions and axionlike pseudoscalar fields (see, e.g., a recent review [17]), the portals are parametrized as $\sqrt{\hbar c}\, g_{a\gamma\gamma} \phi F_{\mu\nu} \tilde{F}^{\mu\nu}$, $\sqrt{\hbar c}\, g_{agg} \phi G_{\mu\nu} \tilde{G}^{\mu\nu}$, and $\sqrt{\hbar c}\, g_{aff} \partial_\mu \phi \bar{\psi}_f \gamma^\mu \gamma^5 \psi_f$, where $F_{\mu\nu}$ and $G_{\mu\nu}$ are Faraday tensors for electromagnetism and QCD, $\tilde{F}_{\mu\nu}$ and $\tilde{G}_{\mu\nu}$ are dual tensors, ψ_f are SM fermionic fields, γ are the Dirac matrices, and g_X are coupling constants. Only the last portal does not conform to the parametrization (1) as it contains the 4-derivative of the axion field. However, when computing action as an integral of the Lagrangian density, the offending 4-derivative $\partial_\mu \phi$ can be moved to the fermion current by integrating by parts, thus restoring the canonical parametrization (1). Further application of the Dirac equation leads to an equivalent form [18] $\partial_\mu \phi \bar{\psi}_f \gamma^\mu \gamma^5 \psi_f \rightarrow 2m_f c^2 \phi \bar{\psi}_f i \gamma^5 \psi_f$, with m_f being the fermion mass. Therefore, the formalism developed in this paper is applicable to direct searches for axionlike particles.

For scalar fields, such as moduli [19–22] and dilatons [23,24], the $\mathcal{O}_X$ in Eq. (1) are scalars. For example, these could be various pieces from the SM Lagrangian density $-\mathcal{L}_{\text{SM}} = \sum_X \mathcal{O}_X$ such as the fermion rest mass energies $m_f c^2 \bar{\psi}_f \psi_f$, electromagnetic Faraday tensor contribution $(1/4) F_{\mu\nu} F^{\mu\nu}$, and gluon field contribution. Quite naturally,

these portals, when combined with the SM Lagrangian, lead to variation of fundamental constants, e.g., the electron rest mass m_e is modulated by the DM field as $m_e(t,\mathbf{r}) = m_{e,0}[1 + \sqrt{\hbar c}\gamma_{m_e}\phi(t,\mathbf{r})]$ or the electromagnetic fine-structure constant $\alpha(t,\mathbf{r}) = \alpha_0[1 + \sqrt{\hbar c}\gamma_\alpha\phi(t,\mathbf{r})]$, where $m_{e,0}$ and α_0 are unperturbed quantities. Virialized ultralight fields oscillate at Compton frequencies, leading to oscillating corrections to fundamental constants. The coupling constants γ_{m_e} and γ_α can be expressed in terms of dimensionless dilaton couplings used, e.g., in Refs. [4,10], $d_e = \gamma_\alpha E_P/\sqrt{2\pi}$ and $d_{m_e} = \gamma_{m_e} E_P/\sqrt{2\pi}$, where the Planck energy $E_P = \sqrt{\hbar c^5/G} \approx 1.22 \times 10^{19}$ GeV.

A typical apparatus takes measurements associated with an operator $\mathcal{O}_X$ (or a combination of operators). For example, an optical clock measures transition frequencies that depend on α (and m_e; see Sec. VII). Then the measured quantity has a DM-induced admixture $S_X(t,\mathbf{r})$ that is proportional to the field value $\phi(t,\mathbf{r})$ at the device location. Thereby, in the assumption of the linear portal, the correlation between two devices' DM signals can be expressed in terms of the two-point DM field correlation function $g(\tau,\mathbf{d}) = \langle\phi(t' = t + \tau, \mathbf{r} = \mathbf{r}' + \mathbf{d})\phi(t,\mathbf{r})\rangle$:

$$\langle S_{X'}(t',\mathbf{r}')S_X(t,\mathbf{r})\rangle \propto \gamma_X\gamma_{X'}\langle\phi(t',\mathbf{r}')\phi(t,\mathbf{r})\rangle.$$

The correlation function for spatiotemporal variations of fundamental constants is also expressed in terms of the DM field correlation function, e.g.,

$$\frac{\langle\alpha(t',\mathbf{r}')\alpha(t,\mathbf{r})\rangle}{(\alpha_0)^2} = 1 + \hbar c(\gamma_\alpha)^2 g(\tau,\mathbf{d}).$$

The derivation of the DM field correlation function $g(\tau,\mathbf{d})$ is the focus of this section. A limiting case of two colocated devices or of the same apparatus is when $d = 0$. Then the correlation function depends on the delay time τ and through the Wiener-Khinchin theorem $g(\tau,0)$ can be related to the DM-induced frequency spectrum of the device. We will derive the dark-matter frequency profile (line shape) in Sec. IV.

B. Derivation of two- and N-point correlation functions

Qualitatively, the VULF's coherence times and coherence lengths are related to DM properties. Indeed, in the standard halo model (see, e.g., Refs. [25,26]), during the galaxy formation, as DM constituents fall into the gravitational potential, their velocity distribution in the galactic reference frame becomes quasi-Maxwellian with a characteristic dispersion (virial) velocity $v_{\rm vir} = \xi c, \xi \approx 10^{-3}$, and a cutoff at the galactic escape velocity. This velocity distribution leads to spectral broadening of oscillations (dephasing) characterized by the coherence time $\tau_c \equiv (\xi^2\omega_\phi)^{-1}$. The velocity distribution also results in a spatial dispersion of individual wave packets, leading to the coherence length $\lambda_c \equiv \hbar/m_\phi\xi c$. All these coherence properties formally emerge from the correlation function derived below.

I derive the VULF correlation function $g(\tau,\mathbf{d})$ by generalizing the formalism of quantum optics to massive spin-0 bosons and the quasi-Maxwellian velocity distribution of DM fields. The major differences from photons are the dispersion relation for massive bosons and the conservation of the total number of particles. In the following two paragraphs, I use natural units for brevity and later restore the fundamental constants. I start the derivation in the galactic reference frame

and then transform the result into the moving device frame. The correlation function is expressed as a trace of field operators and the density matrix $\hat{\rho}$,

$$g(\tau,\mathbf{d}) = \mathrm{tr}[\hat{\rho}\hat{\phi}(t',\mathbf{r}')\hat{\phi}(t,\mathbf{r})].$$

The field operators are $\hat{\phi}(\underline{x}) = \sum_{\mathbf{k}}(\hat{a}_{\mathbf{k}}e^{-i\underline{k}\cdot\underline{x}} + \hat{a}_{\mathbf{k}}^\dagger e^{-i\underline{k}\cdot\underline{x}})/\sqrt{2V\omega_k}$. Here V is the quantization volume, $\underline{k} = (\omega,\mathbf{k})$ and $\underline{x} = (t,\mathbf{r})$ are 4-momentum and 4-position vectors with $\underline{k}\cdot\underline{x}$ denoting their scalar product in flat space-time, and $\hat{a}_{\mathbf{k}}^\dagger$ and $\hat{a}_{\mathbf{k}}$ are bosonic creation and annihilation operators, respectively. The summation is carried out over the field modes with frequencies $\omega_k = \sqrt{m_\phi^2 + \mathbf{k}^2} \approx m_\phi + \mathbf{k}^2/2m_\phi$. The density matrix is defined as $\hat{\rho} = \sum_{\{n_k\}} P(\{n_{\mathbf{k}}\})|\{n_{\mathbf{k}}\}\rangle\langle\{n_{\mathbf{k}}\}|$, where Fock states are $|\{n_{\mathbf{k}}\}\rangle = |n_1, n_2, \ldots\rangle$, with n_k specifying occupation numbers of mode $\mathbf{k}$ and $P(\{n_{\mathbf{k}}\}) = \prod_{\mathbf{k}} P(n_{\mathbf{k}})$ being the probability of finding the ensemble in a particular Fock state. Here $P(n_{\mathbf{k}}) = f_{\rm DM,k}(\mathbf{k})(2\pi)^3/V$, where $f_{\rm DM,k}(\mathbf{k})$ is the DM momentum distribution normalized with respect to $\mathbf{k}$.

Taking into account that the average mode occupation numbers $\bar{n}_{\mathbf{k}}$ are macroscopic and taking the continuous limit,

$$g(\tau,\mathbf{d}) \approx \frac{1}{(2\pi)^3}\int d^3k \frac{1}{\omega_k}\bar{n}_{\mathbf{k}}\cos[\underline{k}\cdot(\underline{x} - \underline{x}')].$$

Here the average mode occupation numbers $\bar{n}_{\mathbf{k}}$ are related to the DM energy density $\rho_{\rm DM}$ and DM momentum distribution as $\bar{n}_{\mathbf{k}} = (2\pi)^3\rho_{\rm DM}f_{\rm DM,k}(\mathbf{k})/m_\phi$. Here I used the fact that for nonrelativistic particles, the number density is $\rho_{\rm DM}/m_\phi$. The requirement that the occupation numbers are macroscopic, $\bar{n}_{\mathbf{k}} \gg 1$, leads to $m_\phi \ll 10$ eV.

The resulting two-point correlation function reads (restoring fundamental constants)

$$g(\tau,\mathbf{d}) = \left(\frac{\hbar}{m_\phi c}\right)^2 \rho_{\rm DM}\int d^3v \frac{f_{\rm DM}(\mathbf{v})}{1 + \frac{1}{2}(\mathbf{v}/c)^2}$$
$$\times \cos\left(\frac{m_\phi c^2}{\hbar}\tau - \frac{m_\phi\mathbf{v}}{\hbar}\cdot\mathbf{d} + \frac{m_\phi\mathbf{v}^2}{2\hbar}\tau\right). \quad (2)$$

Given the DM velocity distribution [27] $f_{\rm DM}(\mathbf{v})$, this expression can be evaluated numerically.

An analytical result can be obtained by taking the Maxwellian distribution of the standard halo model $f_{\rm DM}(\mathbf{v}) = (2\pi)^{-3/2}(\xi c)^{-3}\exp(-\frac{(\mathbf{v}-\mathbf{v}_g)^2}{2(\xi c)^2})$, where ξc is the virial velocity and $\mathbf{v}_g \approx 10^{-3}c$ is the Earth's velocity in the galactic reference frame. We further take the galactic escape velocity cutoff to be infinite and neglect the nonrelativistic kinetic energy correction in the denominator. The resulting correlation function reads

$$g(\tau,\mathbf{d}) \approx \frac{1}{2}\Phi_0^2\mathcal{A}(\tau,\mathbf{d})\cos[\omega_\phi'\tau - \mathbf{k}_g\cdot\mathbf{d} + \Psi(\tau,\mathbf{d})]. \quad (3)$$

Here ω_ϕ' is the Doppler-shifted value of the Compton frequency $\omega_\phi' = \omega_\phi + m_\phi v_g^2/2\hbar$ and $\mathbf{k}_g = m_\phi\mathbf{v}_g/\hbar$ is the "galactic" wave vector associated with the apparatus motion through the dark-matter halo. The effective field amplitude Φ_0 is related to the DM energy density as $\Phi_0 = \frac{\hbar}{m_\phi c}\sqrt{2\rho_{\rm DM}}$, which comes from directly evaluating the temporal (00) component of the stress-energy tensor for the bosonic field. The correlation amplitude

$\mathcal{A}(\tau, \mathbf{d})$ and phase $\Psi(\tau, \mathbf{d})$ are defined as

$$\mathcal{A}(\tau, \mathbf{d}) = \frac{\exp\left(-\frac{|\mathbf{d} - \mathbf{v}_g\tau|^2}{2\lambda_c^2}\frac{1}{1+(\tau/\tau_c)^2}\right)}{[1 + (\tau/\tau_c)^2]^{3/4}},$$

$$\Psi(\tau, \mathbf{d}) = -\frac{|\mathbf{d} - \mathbf{v}_g\tau|^2}{2\lambda_c^2}\frac{\tau/\tau_c}{1+(\tau/\tau_c)^2} + \frac{3}{2}\tan^{-1}(\tau/\tau_c), \quad (4)$$

where the coherence time $\tau_c \equiv (\xi^2\omega_\phi)^{-1} \approx 10^6/\omega_\phi$ and length $\lambda_c \equiv \hbar/m_\phi\xi c$ are expressed in terms of the virial velocity $\xi c \approx 10^{-3}c$. The correlation function encodes the priors on the VULFs and DM halo, such as the DM energy density in the vicinity of the solar system [28], $\rho_{\mathrm{DM}} \approx 0.3$ GeV/cm^3, the motion through the DM halo at $\mathbf{v}_g$, and the virial velocity ξc. Thereby, the correlation function provides an improved statistical confidence in the event of an observation of the DM signal.

The derived correlation function is a *two-point* correlation function, while, in general, a network could have several nodes. The N-point correlation function is expressed in terms of two-point correlation functions. Indeed, the field is composed of a macroscopic number of individual waves [see field operators $\hat{\phi}(\underline{x})$] and, due to the central-limit theorem, the resulting field is Gaussian in nature (see, e.g, Ref. [29]). For Gaussian random fields, the N-point correlation function is fully expressed in terms of the derived two-point correlation function (see, e.g., Appendix E of Ref. [30]). The N-point correlation function vanishes for odd N and for even N is expressed as a sum of all possible products of pairwise two-point correlation functions. For example, for $N_d = 4$ nodes, $\langle\phi(\underline{x}_1)\phi(\underline{x}_2)\phi(\underline{x}_3)\phi(\underline{x}_4)\rangle = g(\underline{x}_1, \underline{x}_2)g(\underline{x}_3, \underline{x}_3) + g(\underline{x}_1, \underline{x}_3)g(\underline{x}_2, \underline{x}_4) + g(\underline{x}_1, \underline{x}_4)g(\underline{x}_2, \underline{x}_3)$, where each of the two-point correlation functions $g(\underline{x}_i, \underline{x}_j) \equiv g(\tau = t_i - t_j, \mathbf{d} = \mathbf{r}_i - \mathbf{r}_j)$ is given by Eq. (3).

Finally, in the limit when both the coherence length λ_c and time τ_c are infinitely large, one recovers the fully coherent wave correlation function

$$g_{\mathrm{coh}}(\tau, \mathbf{d}) = \tfrac{1}{2}\Phi_0^2\cos(\omega_\phi'\tau - \mathbf{k}_g \cdot \mathbf{d}). \quad (5)$$

III. THE VULF PARAMETER SPACE

Now with the correlation function at hand, first we explore the vast VULF parameter landscape. The conversion formulas of VULF masses to Compton frequency, coherence time, and coherence length are, respectively,

$$f_\phi = 2.42 \times 10^5 \left(\frac{m_\phi c^2}{\mathrm{neV}}\right) \mathrm{Hz}, \quad (6)$$

$$\tau_c = 1.59 \times 10^5 \left(\frac{\mathrm{Hz}}{f_\phi}\right) \mathrm{s}, \quad (7)$$

$$\lambda_c = 4.77 \times 10^7 \left(\frac{\mathrm{Hz}}{f_\phi}\right) \mathrm{km}. \quad (8)$$

Typical values of these parameters are compiled in Table I. The coherence time is roughly 10^5 of Compton periods. The coherence length can be interpreted as the de Broglie wavelength of a particle moving at the virial velocity and it is 1000 times larger than the Compton wavelength. The number density of VULF particles $\rho_{\mathrm{DM}}/m_\phi c^2$ ranges from 10^8 to 10^{32} cm^{-3} for the indicated masses in Table I, i.e., a

TABLE I. Parameters of VULF dark matter for a range of masses m_ϕ: Compton frequency f_ϕ, coherence time τ_c and length λ_c, and the inverse galactic wave vector $k_g^{-1} \sim \lambda_c$ associated with the solar system motion through the DM halo.

m_ϕ (eV)	f_ϕ (Hz)	τ_c (s)	λ_c, k_g^{-1} (km)
10^{-24}	2×10^{-10}	7×10^{14}	2×10^{17}
10^{-20}	2×10^{-6}	7×10^{10}	2×10^{13}
10^{-15}	2×10^{-1}	7×10^{5}	2×10^{8}
10^{-10}	2×10^{4}	7×10^{0}	2×10^{3}
10^{-5}	2×10^{9}	7×10^{-5}	2×10^{-2}
1	2×10^{14}	7×10^{-10}	2×10^{-7}

typical device interacts with a macroscopic number of DM particles. Compton frequencies range from nanohertz to petahertz. Notice that one oscillation per year corresponds to $f_\phi = 3 \times 10^{-8}$ Hz (for $m_\phi \sim 10^{-22}$ eV). As points of reference for the coherence length, the size of our galaxy is $\sim 10^{18}$ km and the Earth diameter $\sim 10^4$ km.

IV. DARK-MATTER LINE SHAPE

For a single geographic location, the associated power spectral density (PSD) in frequency space of a coherent signal is a spike at the Doppler-shifted Compton frequency. However, for a stochastic field, the PSD is distributed over a range of frequencies. In this section, I derive the relevant DM-induced spectral line shape. Such a spectral profile can be used as a DM signature.

For a single apparatus, the local temporal correlation the function reads

$$g(\tau, \mathbf{d} = \mathbf{0}) = \frac{1}{2}\Phi_0^2 \frac{\exp\left[-\frac{1}{2}\left(\frac{v_g\tau}{\lambda_c}\right)^2\frac{1}{1+(\tau/\tau_c)^2}\right]}{[1+(\tau/\tau_c)^2]^{3/4}}$$
$$\times \cos[\omega_\phi'\tau + \Psi(\tau, \mathbf{0})]. \quad (9)$$

Notice the presence of the coherence length in the combination $v_g\tau/\lambda_c$; it arises due to our motion through the DM halo over the lag time τ sampling DM fields a distance $v_g\tau \approx 10^{-3}c\tau$ apart. For $\tau = 1$ s this translates into a distance of ~ 300 km. Considering that $v_g \sim v_{\mathrm{vir}}$, $v_g\tau/\lambda_c \sim \tau/\tau_c$. The signal primary oscillation frequency ω_ϕ' also depends on the device galactic velocity v_g through the DM halo via the Doppler shift for massive particles. Since the Earth's velocity changes seasonally, annual velocity modulations are imprinted in the correlation function.

In practice, one could obtain a time series of measurements $\{d_n\}$ at $t_n = nt_0$ and compute the autocorrelation function $G_k = \langle d_n d_{n+k}\rangle$ and see if it fits Eq. (9). A more practical approach, especially for devices exhibiting colored noise, is to work in the frequency space and examine the power spectral density of d_n given by the Fourier transform of G_k. This strategy is formalized in Sec. VI.

To facilitate the frequency-space data analysis, I define the DM-induced line shape as a Fourier transform of the correlation function $f(\omega) = \frac{1}{2\pi}\int_{-\infty}^{\infty} d\tau \, g(\tau, d = 0)e^{i\omega\tau} = \frac{1}{2}\Phi_0^2 F(\omega)$. Here $F(\omega)$ is normalized as $\int_0^\infty F(\omega)d\omega = 1/2$. With $\eta = v_g/v_{\mathrm{vir}} = v_g/\xi c$ and the Doppler-shifted frequency
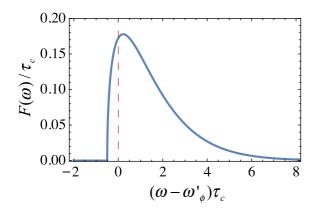
FIG. 2. VULF dark-matter line profile for colocated linear portal-sensitive devices or individual apparatus for $\eta = v_g/v_{\rm vir} = 1$. Dashed vertical line marks the position of the Doppler-shifted Compton frequency $\omega'_\phi = \omega_\phi + m_\phi v_g^2/2\hbar$. The profile value is strictly zero for $\omega < \omega'_\phi - \eta^2/2\tau_c$ due to the dispersion relation for massive particles. The maximum value of $F(\omega) \approx 0.18\tau_c$ is attained at $\omega \approx \omega'_\phi + 0.22/\tau_c$ and the full width at half maximum is $\Delta\omega_\phi \approx 2.5/\tau_c$.

$\omega'_\phi = \omega_\phi + m_\phi v_g^2/2$, the resulting dark-matter line shape reads

$$F(\omega) = (2\pi)^{-1/2}\tau_c\eta^{-1}e^{-\eta^2}e^{-(\omega-\omega'_\phi)\tau_c}$$
$$\times \sinh[\eta\sqrt{\eta^2 + 2(\omega - \omega'_\phi)\tau_c}]. \quad (10)$$

This expression holds for detunings $\omega - \omega'_\phi > -\eta^2/2\tau_c$; otherwise $F(\omega) = 0$. The profile is shown in Fig. 2. As expected, the linewidth is $\sim\tau_c^{-1}$. The profile is strongly asymmetric due to the parabolic dispersion relation for massive non-relativistic bosons: $\omega \approx m_\phi c^2/\hbar + m_\phi \mathbf{v}^2/2\hbar$. The frequency is shifted to the blue for any finite value of velocity $\mathbf{v}$. For the fiducial value of $\eta = 1$, the maximum $F(\omega)$ value of approximately $0.18\tau_c$ is attained at $\omega \approx \omega'_\phi + 0.22/\tau_c$ and the full width at half maximum is $\Delta\omega_\phi \approx 2.5/\tau_c$. The DM line shape is broad in the spectroscopic sense as $\Delta\omega_\phi/\omega_\phi = 3 \times 10^{-6}$.

V. NETWORK

To start the discussion, consider two spatially separated nodes with simultaneously taken measurements so that the two-point correlation function (3) is evaluated at the time lag $\tau = 0$. Figure 3 presents the spatial dependence of such a correlation function for two devices. The spatial dependence is determined by two factors, the correlation length λ_c and the dot product $\mathbf{k}_g \cdot \mathbf{d} = m_\phi \mathbf{v}_g \cdot \mathbf{d}/\hbar$. Because the galactic wave vector is $k_g = \eta/\lambda_c \approx 1/\lambda_c$, the correlation function in Fig. 3 is strongly attenuated, exhibiting only half of an oscillation. This behavior is to be contrasted with the fully coherent correlation function (5). The attenuation is maximal when the device separation vector $\mathbf{d}$ is orthogonal to the galactic velocity $\mathbf{v}_g$ (see blue dashed curve in Fig. 3). In this case, the minor oscillating behavior is entirely due to the phase $\Psi(\tau = 0, \mathbf{d})$ in the two-point correlation function (3).

One could use Fig. 3 as a dark-matter signature. A natural question is how to probe various distances. In galactic coordinates, the Sun moves through the halo in the $(l = 90°, b = 0°)$ direction, roughly towards the Cygnus constellation. The most
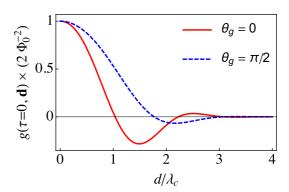

FIG. 3. Spatial dependence of the VULF two-point correlation function for $\eta = v_g/v_{\rm vir} = 1$. The red solid curve illustrates the dependence for the case when the device separation vector $\mathbf{d}$ is aligned with the galactic velocity $\mathbf{v}_g$ and the dashed blue curve when $\mathbf{d} \perp \mathbf{v}_g$. The galactic orientation angle is defined as $\theta_g = \cos^{-1}(\mathbf{k}_g \cdot \mathbf{d})$.

straightforward approach is to place two satellites with, for example, two precision clocks onboard in the vicinity of a Lagrange point, orient their relative position vector $\mathbf{d}$ towards Cygnus constellation [see Fig. 1(b)], and carry out a series of measurements at various distances. This would map out the spatial part of the correlation function.

A more practical approach is to carry out terrestrial experiments [see Fig. 1(c)] with fixed positions of network nodes and rely on the angular dependence of the $\mathbf{k}_g \cdot \mathbf{d} = \cos\theta_g m_\phi v_g d/\hbar$ of the phase. The galactic orientation angle θ_g would change due to the Earth's rotation. The inclination angle of the Cygnus constellation (i.e., the direction of motion through the halo) as seen from the Earth is about $45°$. As an illustration, consider two geographically remote laboratories located along the 45th parallel [see Fig. 1(c)]. Their two-node correlation function would sample $\mathbf{k}_g \cdot \mathbf{d}$ in the range from zero to $k_g d/\sqrt{2}$ over the course of one day. It is worth emphasizing that the coherence length $\lambda_c \sim k_g^{-1}$; thereby two sites have the most sensitivity for $d < \lambda_c$.

The geographic arrangement in Fig. 1(c) serves as an illustrative example as simply time-synchronized measurements in existing laboratories [12] [Fig. 1(a)] should be sufficient for the proposed global data analysis. The GNOME network [31] infrastructure can serve as a natural host for the VULF DM observatory. One could also use clocks on numerous navigational satellites, such as GPS, to search for correlation patterns [14,32]; these have an advantage of half-a-day orbits (GPS) and a large $d \sim 50\,000$ km aperture. The eLISA gravitational wave mission [33] (a network of three satellites) can also be used for VULF detection. Another point is that the network does not need to be homogenous and various precision-measurement tools can be included in the network. Indeed, as long as the DM portal is linear [Eq. (1)], such a global observatory can consider a variety of options on possible DM couplings.

VI. DATA ANALYSIS CONSIDERATIONS

A. Statistical significance of the dark-matter line shape

Now I would like to establish constraints on the coupling constants γ_X of the linear DM-SM portal (1). The temporal data

stream $d_k = s_k + n_k$ is composed of the DM signal s_k and the device noise n_k, $k \in [0, N-1]$. I parametrize the DM signal as $s_k = \gamma_X A \phi(t_k)$, where the constant A depends on the device (see an example for atomic clocks in Sec. VII) and $t_k = k \Delta_t$ refers to the time of the measurement k, with Δ_t being the sampling interval. For simplicity, I assume that the network is fixed in the halo reference frame; otherwise the positions of the terrestrial nodes would need to be tracked and the time series transformed. The noise quasi-PSD is defined as $\tilde{\rho}_p = \langle |\tilde{n}_p|^2 \rangle$, where $\tilde{n}_p$ stands for the discrete Fourier transformed (DFT) set of n_k, $\tilde{n}_p = \sum_{k=0}^{N-1} \exp(-i \frac{2\pi}{N} kp) n_k$. A review of the discrete Fourier transform can be found in Appendix A 1. The DM signal PSD can be expressed as $\langle |\tilde{s}_p|^2 \rangle = A^2 \gamma_X^2 \langle |\tilde{\phi}_p|^2 \rangle$, which can be further linked to the profile (10) via

$$\langle |\tilde{\phi}_p|^2 \rangle = \frac{\pi N}{\Delta_t} \Phi_0^2 F(\omega_p), \qquad (11)$$

as long as there is no the DFT-inherent aliasing (see Sec. VI B). Here $\omega_p = \frac{2\pi}{N \Delta_t} p$ is the DFT angular frequency.

The probability density for the field DFT coefficients is given by (see Appendix A 3)

$$p(\tilde{\boldsymbol{\phi}}) = \prod_{p=0}^{N/2} \frac{1}{(\beta_p^{-1} \pi \langle |\tilde{\phi}_p|^2 \rangle)^{\beta_p}} \exp\left(-\beta_p \frac{|\tilde{\phi}_p|^2}{\langle |\tilde{\phi}_p|^2 \rangle}\right). \qquad (12)$$

In this expression, $\tilde{\boldsymbol{\phi}}$ is a vector composed of the field DFT components $\tilde{\phi}_p$, and $\beta_j = 1$ except for the dc and the Nyquist components for which $\beta_0 = \beta_{N/2} = 1/2$. A particular field realization can be constructed by randomly drawing coefficients $\tilde{\phi}_p$ from the distribution (12) and using the inverse discrete Fourier transform $\phi_k = N^{-1} \sum_{p=0}^{N-1} \exp(i \frac{2\pi}{N} kp) \tilde{\phi}_p$. The cause for the field decoherence is dephasing when multiple oscillations of different frequencies are added together.

The relevant likelihood for a stochastic signal is given by Eq. (A17). It is obtained by multiplying the DFT likelihood for a noisy device and a DM signal with fixed (deterministic) $\tilde{\boldsymbol{\phi}}$ with the field probability distribution (12) and marginalizing over $\tilde{\boldsymbol{\phi}}$. The resulting stochastic signal likelihood can be recast into a posterior probability density for the coupling strength γ_X. As shown in Appendix B, in the weak signal limit, the maximum-likelihood estimator for γ_x reads

$$\hat{\gamma}_X^{(1)} = A^{-1} \left\{ \frac{\sum_{p=1}^{N/2-1} \frac{\langle |\tilde{\phi}_p|^2 \rangle}{\tilde{\rho}_p} \left(\frac{|\tilde{d}_p|^2}{\tilde{\rho}_p} - 1\right)}{\sum_{p=1}^{N/2-1} \left(\frac{\langle |\tilde{\phi}_p|^2 \rangle}{\tilde{\rho}_p}\right)^2 \left(2 \frac{|\tilde{d}_p|^2}{\tilde{\rho}_p} - 1\right)} \right\}^{1/2}, \qquad (13)$$

with the standard deviation

$$\hat{\sigma}_{\gamma_X}^{(1)} \approx A^{-1} \left\{ \sum_{p=1}^{N/2-1} \left(\frac{\langle |\tilde{\phi}_p|^2 \rangle}{\tilde{\rho}_p}\right)^2 \left(2 \frac{|\tilde{d}_p|^2}{\tilde{\rho}_p} - 1\right) \right\}^{-1/4}. \qquad (14)$$

To streamline the notation, here I assumed that the dc ($p = 0$) and the Nyquist ($p = N/2$) components of the time series have been removed or filtered out. Further averaging (14) over multiple data realizations leads to an estimate

$$\sigma_{\gamma_X}^{(1)} \approx A^{-1} \left\{ \sum_{p=1}^{N/2-1} \left(\frac{\langle |\tilde{\phi}_p|^2 \rangle}{\tilde{\rho}_p}\right)^2 \right\}^{-1/4}. \qquad (15)$$

The constraint on $|\gamma_X|$ at the 68% confidence level is $|\gamma_X| < \sigma_{\gamma_X}^{(1)}$. An immediate consequence of Eq. (15) is that the constraints on $|\gamma_X|$ scale with the number of frequency points N_F sampled inside the DM line shape (Fig. 2) as $1/N_F^{1/4}$. This is a qualitatively expected result, since the standard deviation of an average of N_F data points (here the measured quantity is the VULF signal PSD) scales as $1/\sqrt{N_F}$. The additional square root comes from the fact that the VULF signal PSD is proportional to $(\gamma_X)^2$. The number of points inside the profile N_F is on the order of $(\tau_c \Delta_f)^{-1}$, where $\Delta_f = 1/N \Delta_t$ is the DFT frequency step. Thus $N_F \sim N \Delta_t / \tau_c$.

The constraint (15) can be simplified further for white-noise devices (see Appendix C for details). For white noise, the PSD is flat, $\tilde{\rho}_p = N \sigma^2$, with σ being the noise standard deviation. For the fiducial value of $\eta = 1$,

$$|\gamma_X| < 2.4 \frac{\sigma}{A \Phi_0} \left(\frac{\Delta_t}{N \tau_c}\right)^{1/4}, \qquad (16)$$

which formalizes the earlier qualitative observations. The factor $(\Delta_t / \tau_c)^{1/4}$ can be substantial: For Compton frequencies on the order of the sampling rate it is $O(\xi^{1/2}) \approx 3 \times 10^{-2}$. For a fixed duration of a measurement campaign, the tightest bounds are obtained for $\Delta_t \sim \tau_c$. The constraints can be further reexpressed in terms of boson masses and DM energy density

$$|\gamma_X| < 5.4 \times 10^{-2} \frac{\sigma}{A} \frac{m_\phi c}{\hbar \sqrt{\rho_{\mathrm{DM}}}} \left(\frac{m_\phi c^2}{\hbar N} \Delta_t\right)^{1/4}, \qquad (17)$$

revealing the $m_\phi^{5/4}$ scaling when the device constant A does not depend on the Compton frequency.

Now we consider a special case of a fully coherent signal, i.e., $\tau_c \gg N \Delta_t$. Then the field $\phi(t) = \Phi_0 \cos(\omega_\phi t + \varphi)$, where φ is some random but fixed phase. For illustration, take ω_ϕ to be equal to one of the DFT angular frequencies, say, ω_m, $0 < m < N/2$. Then the field PSD $\langle |\tilde{\phi}_p|^2 \rangle = \frac{1}{4} \Phi_0^2 N^2 \delta_{p,m}$ and, for white noise, Eq. (15) reduces to

$$|\gamma_X| < \sigma_{\gamma_X}^{(1),\mathrm{coh}} \approx \frac{\sigma}{A \Phi_0} \frac{2}{\sqrt{N}}. \qquad (18)$$

Thus comparing the stochastic field (16) and the coherent field (18) constraints, we see that the sensitivity in the stochastic field case differs by a factor $(N \Delta_t / \tau_c)^{1/4}$. This is in contradiction to the statement made in Ref. [4] (using the notation of this paper) that "we expect to boost the sensitivity σ of a single measurement by a factor of $[\min(N, \tau_c/\Delta_t)]^{1/2}$—the square root of the number of coherent measurements." The correct statement would have included the factor of $(N \tau_c / \Delta_t)^{1/4}$ instead of $(\tau_c / \Delta_t)^{1/2}$ [see Eqs. (16) and (18) for additional $O(1)$ numerical factors]. While the derived scalings are consistent with magnetometry sensitivity estimates [7], they apply to a broader range of experiments and include numerical factors specific to DM velocity distributions.

Based on Eqs. (13) and (14), one could also devise the signal-to-noise ratio (SNR) $\mathcal{S}$ statistic in frequency space

$$\mathcal{S} \equiv \frac{\hat{\gamma}_X^{(1)}}{\hat{\sigma}_{\gamma_X}^{(1)}} \qquad (19)$$

that can be applied to the data streams directly. This is an application of the matched filter technique (for example,

used by the gravitational wave community [34]). The specific values of the VULF PSD $\langle|\tilde{\phi}_p|^2\rangle$ template depend on the field Compton frequency. Thus the SNR statistic needs to be scanned against multiple templates by varying f_ϕ and searching for $\mathcal{S}$ values to exceed a certain value, e.g., $\mathcal{S} > 5$.

One of the subtleties is that, while deriving formulas in this section, the device noise PSD $\tilde{\rho}_p$ was assumed to be known. The VULFs are, however, ever-present and cannot be turned off or shielded out. A strategy could be to fit the data PSD with a smooth polynomial and assign the noise PSD to the smooth background. In addition, more sophisticated, Bayesian logic-based approaches can be adopted; see, e.g., the mixture model discussion in Ref. [35].

Finally, it is worth noting that Eqs. (16) and (17) were derived under the assumption that the entire DM line shape is sampled in the DFT frequency space, i.e., nominally for VULF frequencies below the DFT Nyquist frequency. However, as shown in the following section, this limitation can be substantially relaxed and the sensitivity to Compton frequencies above the Nyquist frequency can be gained due to *aliasing* inherent to the discrete Fourier transform. I will demonstrate that the sensitivity estimates (16) and (17) hold for $f_\phi \lesssim 10^6/2\pi\Delta_t$.

B. Probing high-frequency dark-matter fields through aliasing

A high-frequency (above the Nyquist frequency) DM field still interacts with the device, but it is just sampled at an insufficient rate to resolve individual field oscillations. The aliasing in discrete sampling qualitatively refers to the fact that the PSD of an oscillation of frequency ω_ϕ and that of the same amplitude and phase oscillations of frequencies $\omega_\phi + (2\pi/\Delta_t)q$, with q being an integer, are identical. In other words, the DM oscillations with frequencies above the Nyquist frequency are effectively shifted to the nominal DFT range: $f_{\phi,\text{aliased}} = \text{mod}\,(f_\phi, 1/\Delta_t)$. To explicitly demonstrate this relation, examine the statement of the Wiener-Khinchin theorem in DFT space relating the PSD and the time-domain correlation function

$$\langle|\tilde{\phi}_p|^2\rangle = N \sum_{k=-(N-1)}^{N-1} \exp\left(-i\frac{2\pi}{N}pk\right)g(k\Delta_t,\mathbf{0}). \quad (20)$$

It can be verified by a direct substitution in Eq. (9) that $g(k\Delta_t,\mathbf{0})$ is invariant under $\omega'_\phi \rightarrow \omega'_\phi + (2\pi/\Delta_t)q$.

Figure 4 demonstrates the aliasing effect on the sampled DM field PSD for various Compton frequencies. In this figure, to generate the field PSDs, I carried out summations in the Wiener-Khinchin theorem (20) numerically with the two-point correlation function (9), setting $v_g = v_{\text{vir}}$. The coherence time τ_c was varied with Compton frequency according to Eq. (7). In this simulation, the total number of points and the sampling interval were $N = 2 \times 10^6$ and $\Delta_t = 0.1$ s, respectively. The corresponding Nyquist frequency is $f_{\text{Nyquist}} = 1/2\Delta_t = 5$ Hz. Several observations can be made based on this simulation.

(i) While the high-frequency fields are aliased to the nominal DFT frequency range, the original coherence time is retained by the aliased copy. Therefore, an experimentalist should search for aliased VULF lines that may be broader than the ones expected from the VULF oscillations in the nominal $0 \leqslant f_\phi \leqslant f_{\text{Nyquist}}$ frequency range.
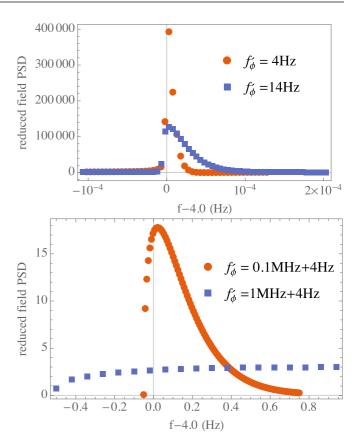

FIG. 4. Effects of DFT aliasing on the observable power spectral density of dark-matter field. Reduced PSD is defined as $\langle|\tilde{\phi}_p|^2\rangle/N\Phi_0^2$ and is shown as a function of DFT frequency detuning from 4 Hz. The aliased Doppler-shifted Compton frequency for all curves is 4 Hz. The Nyquist frequency in the simulation is 5 Hz. See the text for other simulation parameters. The top panel is for low-frequency Doppler-shifted Compton frequencies and the bottom panel shows PSDs for high-frequency fields. The data sampling rate is the same for all shown curves.

(ii) The shape of the DM line is preserved as long as the bulk of the aliased profile fits inside the nominal DFT frequency range $0 \leqslant f \leqslant f_{\text{Nyquist}}$. If $\tau_c \lesssim \Delta_t$, the shape is distorted by the aliasing and the background-signal separation becomes challenging. An example of such a distortion is for the $f'_\phi = 1$ MHz + 4 Hz curve in Fig. 4. This observation, in particular, means that the sensitivity estimates (16) and (17) hold for $f_\phi \lesssim 10^6/2\pi\Delta_t$.

(iii) The nondistortion condition $\tau_c \lesssim \Delta_t$ means that the VULF field must remain coherent over a duration of a sampling period.

Suppose that the total observation time $T = N\Delta_t$ is smaller than the coherence time for a Compton frequency that is below f_{Nyquist}. Then this oscillation behaves as a deterministic coherent signal on the timescale T. As we start searching for higher Compton frequencies via aliasing, the DM signal becomes increasingly stochastic in nature, with coherence time on the order of the sampling time Δ_t for the highest probed frequencies. Then the stochastic field approach developed in this paper, while being valid for deterministic signals, becomes especially relevant. Statistical estimators (13)–(15) explicitly refer to the DM field PSD $\langle|\tilde{\phi}_p|^2\rangle$. In practice, these quantities

should be estimated using DFT sampling (20) of the correlation function to properly reflect aliasing and the accompanying distortions. Notice that the use of Doppler-shifted frequencies for high-frequency fields is important, because aliased frequencies are mapped as mod $(f'_\phi, 1/\Delta_t)$, and $1/\Delta_t$ may be comparable to the Doppler shift $m_\phi v_g^2/4\pi\hbar$.

Aliasing effects extend the DM searches to higher Compton frequencies, as long as the frequencies of VULF oscillations are within the device bandwidth. This idea was previously employed in Ref. [11] to establish projected high-frequency constraints on VULF coupling strengths in atom interferometry.

C. Statistical significance of the correlation function for a network

Section VI A established constraints on the coupling strength γ_X for a single device. The derivation for a multinode network is similar, starting from the network likelihood (A22) (see Appendix A 4 for details). I label the devices with the letters at the beginning of the alphabet $a, b, c, \ldots$ and operate with N_d-dimensional quasi-PSD matrices $\boldsymbol{\rho}_p$ and $\boldsymbol{S}_p$, where the index p, as previously, refers to the DFT frequency. The noise and the DM signal PSD matrices $\boldsymbol{\rho}_p$ and $\boldsymbol{S}_p$ have elements in the node space $\rho_p^{a,b} = \langle \tilde{n}_p^a (\tilde{n}_p^b)^* \rangle$ and $S_p^{a,b} = \gamma_X^2 A^2 \langle \tilde{\phi}_p^a (\tilde{\phi}_p^b)^* \rangle$, respectively. Here $\tilde{n}_p^a$ is the DFT component of the ath device noise and $\tilde{\phi}_p^a$ is the DFT component of the field at the location $\mathbf{r}^a$ of the ath device. If the devices are independent, i.e., their noise is mutually uncorrelated and the devices are identical, $\rho_p^{a,b} = \delta_{a,b} \tilde{\rho}_p$. The quantities $\Phi_p^{a,b} \equiv \langle \tilde{\phi}_p^a (\tilde{\phi}_p^b)^* \rangle$ are related through the Fourier transform (the Wiener-Khinchin theorem) to the derived two-point correlation function $g(\tau, \mathbf{d}^{a,b} = \mathbf{r}^a - \mathbf{r}^b)$.

The resulting standard deviation for the coupling strength γ_X in the weak DM signal limit reads

$$\sigma_{\gamma_X}^{(\text{network})} = A^{-1} \left\{ \sum_{p=1}^{N/2-1} \frac{\text{tr}(\boldsymbol{\Phi}_p \boldsymbol{\Phi}_p)}{(\tilde{\rho}_p)^2} \right\}^{-1/4}. \quad (21)$$

The major difference from the single device formula (15) is the presence of the trace $\text{tr}(\boldsymbol{\Phi}_p \boldsymbol{\Phi}_p) = \sum_{a,b} \Phi_p^{a,b} \Phi_p^{b,a}$. If all N_d nodes are separated by distances larger than the coherence length λ_c, only the diagonal elements contribute to the trace and $\sigma_{\gamma_X}^{(\text{network})} = \sigma_{\gamma_X}^{(1)}/N_d^{1/4}$, where $\sigma_{\gamma_X}^{(1)}$ is the standard deviation for a single device (15).

In the opposite limit of the node separations being much smaller than λ_c, $\sigma_{\gamma_X}^{(\text{network})} = \sigma_{\gamma_X}^{(1)}/\sqrt{N_d}$. Thus, compared to an individual device, the statistical sensitivity of a fully coherent network is improved by the factor $\sqrt{N_d}$, where N_d is the number of nodes. The qualitative reason for this scaling is that at each DFT frequency, the network samples $(N_d)^2$ DM quantities $S_p^{a,b}$. Due to the conventional $1/\sqrt{\mathcal{N}}$ (where $\mathcal{N}$ denotes the number of data points) averaging dependence, this leads to $\sigma_{\gamma_X}^{(\text{network})} \propto 1/\sqrt{N_d}$. An additional square root comes from the fact that each of the measured quantities $S_p^{a,b}$ is proportional to $(\gamma_X)^2$.

The best bounds are attained for colocated devices or the fully coherent network, i.e., when $d^{a,b} \ll \lambda_c$. Indeed, in this case in Eq. (21) all cross-node correlators are equal to a single-node correlator: $\Phi_p^{a,b} = \Phi_p^{a,a}$. For a distributed network,

however, $\Phi_p^{a,b} \leqslant \Phi_p^{a,a}$ and the statistical sensitivity is reduced and is bounded by the case when $d^{a,b} \gg \lambda_c$ for all the network links:

$$\sigma_{\gamma_X}^{(1)}/(N_d)^{1/2} \leqslant \sigma_{\gamma_X}^{(\text{network})} \leqslant \sigma_{\gamma_X}^{(1)}/(N_d)^{1/4}.$$

An experiment operating at a hertz sampling rate probes subhertz Compton frequencies (see, however, Sec. VI B for the possibility of probing higher frequencies), which translate into coherence lengths [Eq. (8)] $\lambda_c \gtrsim 5 \times 10^7$ km. Thus even a global terrestrial network ($d^{a,b} \lesssim 10^4$ km) of such devices would operate in the fully coherent regime, gaining the most in sensitivity from the correlated analysis: $\sigma_{\gamma_X}^{(\text{network})} = \sigma_{\gamma_X}^{(1)}/\sqrt{N_d}$. This condition, however, can change for higher-frequency fields with shorter coherence times probed through the aliasing technique. For example, for a megahertz field, the coherence length is ~ 10 km.

VII. ATOMIC CLOCKS

In this section, I qualitatively discuss an application of the presented formalism to atomic clocks and their networks.

In our preceding discussion we assumed that the measurements were instantaneous; in practice, there is always a finite interrogation time t_0 for a single measurement. I assume that the next measurement is taken right after the previous one was completed (no dead times), with the DFT sampling time interval of Sec. VI $\Delta_t = t_0$. We form a time series of fractional frequency excursions $s_n^{(a)} \equiv (\omega_n - \omega_c)/\omega_c$ taken at $t_n = nt_0$; $n = \overline{1, N}$ for a fixed internode distance d, with a labeling the node and ω_c being the nominal clock frequency. The VULF contribution to $s_n^{(a)}$ can be expressed in terms of the single-measurement accumulated clock phase and sensitivity coefficients $K_X = \partial \ln \omega_c / \partial \ln X - \partial \ln \omega_{\text{LO}} / \partial \ln X$, where ω_{LO} is the resonance frequency of the local oscillator (reference cavity):

$$s_n^{(a)} = \left(\sqrt{\hbar} c \sum_X \gamma_X K_X \right) \int_{t_n - t_0}^{t_n} \phi(\mathbf{r}^a, t') \frac{dt'}{t_0}. \quad (22)$$

Notice the integral of the VULF field time evolution history over the interrogation duration. In this section, X runs over fundamental constants that affect the atomic or the local oscillator resonance frequencies. The constants may include the electromagnetic fine-structure constant α, the mass of the electron m_e, and so on (see, e.g., the discussion in [32] for both optical and microwave clocks). To streamline the notation, we combine $\sum_X \gamma_X K_X = \gamma_{\text{eff}}$, and γ_X is to be replaced with γ_{eff} in the previous sections.

The reference to the dependence of the local cavity resonance frequency ω_{LO} on fundamental constants in the sensitivity coefficients K_X is due to the fact that in the Ramsey interrogation scheme, the accumulated atomic phase and thus the detected quantum probability of a resonant transition is determined by a time integral of the difference in frequencies between the clock atom and the local oscillator. The local oscillator (reference cavity) itself is subject to the DM field influence during the interrogation. An example of such an effect is the DM-induced variation in the Bohr radius $a_0 = \alpha\hbar/m_e c$ affecting the cavity length $L \propto a_0$ and thus the cavity

resonance frequencies [9]. I refer the reader to further clock-specific discussions in [32,36].

Equation (22) is an approximation as it assumes instantaneous responses of the atom and the local oscillator to the time-varying fundamental constants. In particular, the cavity response is not instantaneous, for example, due to the laser pulse intracavity round-trip time $2L/c$ being finite. Moreover, the macroscopic adjustment of the macroscopic cavity length to the microscopic variations of fundamental constants requires propagation of sound waves in the cavity spacer material [10] and therefore the cavity dynamic response can exhibit a frequency cutoff above the characteristic frequency $v_s/L \sim 10^5$ Hz, where v_s is the speed of sound in the cavity spacer. The dynamic response of an atom is much faster, with an expected qualitative change in the otherwise nearly instantaneous response behavior above typical atomic frequencies, which are comparable to the upper limit on the plausible values of Compton frequencies (see Table I). Thereby, in general, the sensitivity coefficients K_X also depend on time and, strictly speaking, should include the delayed cavity response. Another subtlety is an operation of the atomic clock servoloop that locks the cavity resonance to the atomic frequency and requires several measurement cycles (see Ref. [32]).

It is worth mentioning that it is hardly necessary to make frequency ratio comparisons between clocks of different sensitivities to the variation of fundamental constants as in the original proposal [4] and the follow-up experimental work [37,38]. The frequency comparison of a local oscillator and the clock atoms is naturally carried out per the conventional operation of a single atomic clock and it is sufficient. Another advantage of using a single clock is a larger sensitivity to the variation of fundamental constants (see also Ref. [11]). For both microwave and optical clocks $\partial \ln \omega_c / \partial \ln \alpha \approx 2$ due to the Rydberg constant being $\alpha^2 m_e c^2$. In the frequency-ratio technique, however, this dominant contribution cancels out and the sensitivity is attributed entirely to the small difference in α-dependent relativistic corrections to atomic structure.

Now, assuming the validity of Eq. (22), consider a measurement with a single clock. If the DM field remains coherent over a duration of a single measurement $t_0 \ll \tau_c$, the field behaves as $\phi(\mathbf{r}^a, t) \approx \Phi_0 \cos(\omega'_\phi t + \varphi^a)$ over t_0, where the phase $\varphi^a = \varphi - \mathbf{k} \cdot \mathbf{r}^a$, with φ being a fixed phase common to all nodes. Then the VULF signal [Eq. (22)] is explicitly

$$s_n^{(a)} = \sqrt{\hbar c}\, \gamma_{\text{eff}} \frac{\sin(\omega'_\phi t_0/2)}{\omega_\phi t_0/2} \phi(\mathbf{r}^a, t_{n-1} + t_0/2), \qquad (23)$$

leading to the identification of the device constant A of Sec. VI as $A = \sqrt{\hbar c}\, \mathcal{W}(\omega'_\phi t_0)$, where the filter function is

$$\mathcal{W}(\omega'_\phi t_0) = \frac{\sin(\omega'_\phi t_0/2)}{\omega'_\phi t_0/2}. \qquad (24)$$

This function emphasizes the dependence on the ratio of the interrogation time to the period of VULF oscillation. If VULF oscillations are slow compared to t_0, then $\mathcal{W}(\omega'_\phi t_0 \ll 1) \approx 1$, and if they are fast, the effect tends to average out, $|\mathcal{W}(\omega'_\phi t_0 \gg 1)| < 2(\omega'_\phi t_0)^{-1}$. For a typical [39] $t_0 \sim 1$ s for optical lattice clocks, the separation between the two regimes occurs at $f_\phi \approx 1$ Hz ($m_\phi \sim 10^{-14}$ eV). For the nominally probed Compton frequencies $f_\phi < 1/2t_0$, the influence of

the window function is minimal, $\mathcal{W}(\omega'_\phi t_0) \approx 1$. However, the bandwidth-limiting effect of the filter function becomes important for higher frequencies probed through the aliasing technique (Sec. VIB). The condition $t_0 \ll \tau_c$ employed in deriving Eq. (23) is consistent with the limits on applicability of the aliasing technique, $f_\phi \lesssim 10^6/2\pi t_0$. For our illustrative optical lattice clock example with $t_0 = 1$ s, $f_\phi \lesssim 0.2$ MHz ($m_\phi \lesssim 8 \times 10^{-10}$ eV).

The search in the indicated VULF frequency parameter space can be carried out by directly employing the frequency-space SNR statistic of Sec. VIA. If the $\mathcal{S} < 1$ for the entire probed frequency space, one could rigorously constrain the coupling constant γ_{eff} through Eq. (15) for the measured clock noise PSD.

An estimate of the sensitivity can be made by assuming that the measurement noise is dominated by the white frequency noise, i.e., Allan variance scales as $\sigma_y(\tau) \propto 1/\sqrt{\tau}$. The associated noise PSD is flat. Then σ in Eq. (17) can be replaced by the Allan variance $\sigma_y(t_0)$, leading to the constraint on the effective coupling strength

$$|\gamma_{\text{eff}}| < 5.4 \times 10^{-2} \frac{\sigma_y(t_0)}{|\mathcal{W}(\omega_\phi t_0)|} \frac{m_\phi c^{1/2}}{\hbar^{3/2} \sqrt{\rho_{\text{DM}}}} \left(\frac{m_\phi c^2}{\hbar N} t_0 \right)^{1/4}. \qquad (25)$$

This estimate holds for $t_0 \ll \tau_c$ and $\tau_c \ll N t_0$. For low frequencies $\tau_c \gg N t_0$, one needs to employ the properly adopted Eq. (18).

The projected constraints on the electromagnetic gauge modulus d_e are shown in Fig. 5. I used the value of $\sigma_y(1\text{ s}) = 10^{-16}$, characteristic of modern optical cavities [40]. I set $K_\alpha = 3$ and suppressed sensitivity to the electron mass variation $d_{m_e} \equiv 0$. Then $\gamma_{\text{eff}} = 3\gamma_\alpha = 3\sqrt{2\pi}d_e/E_{\text{P}}$, where the last relation is for the electromagnetic gauge modulus d_e (see Sec. IIA). For high ($f'_\phi > 1/t_0$) frequencies I set $|\mathcal{W}(\omega'_\phi t_0)| = 2(\omega'_\phi t_0)^{-1}$ as one could simply repeat the experiment with a slightly
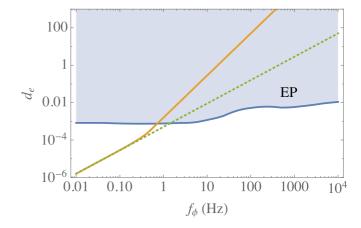

FIG. 5. Projected constraints on the electromagnetic gauge modulus d_e for high Compton frequencies. The excluded parameter space from the equivalence principle (EP) tests [10] is shown as a shaded region. The solid orange line is the projected limit from Eq. (25) for an optical clock compared to the state-of-the-art cavity [40] (see the text for details). The dashed green line is drawn neglecting the bandwidth-limiting effect of the filter function (24).

adjusted t_0 to maximize sensitivity for a given ω'_ϕ. The single measurement time t_0 was set to 1 s and one year of integration time was assumed. In Fig. 5 there is a region of parameter space where the clocks can explore yet-unconstrained parameter space. The existing equivalence principle constraints on the modulus d_{m_e} are about an order of magnitude worse than those for d_e [10], somewhat improving the discovery reach of atomic clocks. To improve the sensitivity, one needs to improve the short-term clock stability. While in the region of high frequencies, resonant mass detectors may be more competitive [10], but are narrow band.

The constraints can be improved further by employing a network of clocks. The global clock networks include the global positioning system and other navigational satellite constellations and a trans-European network of laboratory clocks [41,42]. Navigational satellites house microwave clocks on board and the navigational systems also include clocks on terrestrial stations. Several local clock networks are available at national metrology institutes around the world, mostly used for clock comparisons. It is clear from the discussion in Sec. VIC that compared to an individual clock, the statistical sensitivity of a network is improved by a factor of up to $\sqrt{N_d}$, where N_d is the number of clocks. The best limits on γ_X are attained when the clocks are colocated (or within the field coherence length), but, in the event of a positive observation, the confidence is improved for a distributed network.

VIII. CONCLUSION

Examination of the VULF parameter space in Table I raises the question of when the DM signal can be considered deterministic and when it is stochastic in nature. If the total measurement time is below the coherence time, then the VULF behaves as a deterministic oscillating signal. While the phase, the amplitude, and the frequency of the oscillations are randomly drawn from the probability distribution (12), their values persist over the entire measurement duration. If, however, the duration of the measurement campaign is much longer than the VULF coherence time, then multiple field realizations are sampled and one needs to apply the stochastic field techniques discussed in this paper. The stochastic approach becomes even more valuable when the high-frequency fields are probed through the aliasing effect inherent to discrete sampling, as the coherence time becomes shorter for such fields. The presented formalism is applicable to both cases and can serve as a starting point for statistical analysis.

This paper established a theoretical formalism for analyzing stochastic properties of ultralight dark-matter fields through an explicit evaluation of the DM field N-point correlation function. The correlation function encodes all so-far-established DM priors. For a single device, I derived a DM line-shape profile than can be directly compared to the experimental data through the developed SNR statistic. The paper also addressed the DM sensitivity of a distributed (or colocated) network of precision-measurement tools.

APPENDIX A: DISCRETE FOURIER TRANSFORM AND FREQUENCY-SPACE PROBABILITY DISTRIBUTIONS FOR DETERMINISTIC AND STOCHASTIC SIGNALS

1. Review of the discrete Fourier transform

Introductions to the discrete Fourier transform can be found, for example, in Refs. [34,43]. Here we review key definitions and relevant results and also introduce the notation used through the main text of the paper.

Consider a time series $\{x_k\}$ with values tabulated at times $t_k = k\Delta_t$, $k = \overline{0, N-1}$. The total observation time is $T = N\Delta_t$, where N is the total number of individual measurements and Δ_t is the time step. We will assume that N is an even number and x_k are real valued. The discretized time series is continued periodically outside the observation time interval.

The DFT components $\tilde{x}_p$ are defined via the discretized Fourier transformation of the time series

$$\tilde{x}_p = \sum_{k=0}^{N-1} \exp\left(-i\frac{2\pi}{N}pk\right)x_k. \tag{A1}$$

The index p refers to the DFT frequencies $f_p = p/N\Delta_t$ or, equivalently, to the DFT angular frequencies $\omega_p = 2\pi f_p$. The frequency steps are $\Delta_f \equiv 1/N\Delta_t$ and $\Delta_\omega \equiv 2\pi/N\Delta_t$.

Introducing vectors $\mathbf{x} = \{x_0, x_1, \ldots, x_{N-1}\}^T$ and $\tilde{\mathbf{x}} = \{\tilde{x}_0, \tilde{x}_1, \ldots, \tilde{x}_{N-1}\}^T$, the discrete Fourier transform can be interpreted as a linear transformation (basis rotation)

$$\tilde{\mathbf{x}} = \sqrt{N}\boldsymbol{U}\boldsymbol{x}, \tag{A2}$$

where the elements of the matrix $\boldsymbol{U}$ are $U_{pk} = \frac{1}{\sqrt{N}}\exp(-i\frac{2\pi}{N}pk)$. The transformation matrix $\boldsymbol{U}$ is symmetric, $\boldsymbol{U}^T = \boldsymbol{U}$, and unitary, $\boldsymbol{U}^{-1} = \boldsymbol{U}^\dagger$. Using unitarity, Eq. (A2) can be inverted to yield the inverse discrete Fourier transform

$$\boldsymbol{x} = (\sqrt{N})^{-1}\boldsymbol{U}^\dagger\tilde{\mathbf{x}}. \tag{A3}$$

Discrete Fourier transformed values are periodic, $\tilde{x}_{N+p} = \tilde{x}_p$, as can be verified directly from Eq. (A1). Thereby, we limit p to the nominal range $\overline{0, N-1}$ with frequencies f_p ranging from 0 to $(N-1)/N\Delta_t$. Since $\mathbf{x}$ are real valued

$$\tilde{x}_p = \tilde{x}_{-p}^* = \tilde{x}_{N-p}^*. \tag{A4}$$

Clearly, the information contained in coefficients $\tilde{x}_p$ at frequencies above the Nyquist frequency $f_{\text{Nyquist}} = f_{N/2} = 1/2\Delta_t$ is redundant as these coefficients can be recovered by complex

conjugating coefficients of frequencies below f_{Nyquist}. Another consequence of Eq. (A4) is that the dc $\tilde{x}_0$ and the Nyquist $\tilde{x}_{N/2}$ DFT components are strictly real valued: $\tilde{x}_0 = \sum_{k=0}^{N-1} x_k = N\langle x \rangle$ and $\tilde{x}_{N/2} = \sum_{k=0}^{N-1} (-1)^k x_k$.

If **x** is a stochastic time series, we may define the autocorrelation matrix **C** with elements $C_{kk'} = \langle x_k x_{k'} \rangle$. For stationary processes, the autocorrelation depends only on the lag $l = k' - k$, so $C_l \equiv C_{k,k+l} = \langle x_k x_{k+l} \rangle$. Then the autocorrelation function has the following properties: $C_0 = \langle x_k x_k \rangle = \sigma^2$, $C_l = C_{-l}$, and $|C_l| \leqslant C_0 = \sigma^2$, where σ is the standard deviation.

We define the (two-sided) PSD matrix $\tilde{\mathbf{C}}$ with elements $\tilde{C}_{pp'} \equiv \langle \tilde{x}_p (\tilde{x}_{p'})^* \rangle$, which by using (A2) can be related to the autocorrelation matrix **C** as

$$\tilde{\mathbf{C}} = N\mathbf{U}\mathbf{C}\mathbf{U}^\dagger, \qquad (A5)$$

$$\mathbf{C} = N^{-1}\mathbf{U}^\dagger\tilde{\mathbf{C}}\mathbf{U}. \qquad (A6)$$

For stationary processes, the PSD matrix is diagonal: $\tilde{C}_{pp'} = \delta_{pp'}\langle |\tilde{x}_p|^2 \rangle$. We will simply refer to the diagonal matrix elements as $\tilde{C}_p \equiv \langle |\tilde{x}_p|^2 \rangle$. In particular,

$$
\begin{aligned}
\tilde{C}_p &= N \sum_{kk'} U_{pk} C_{kk'} U_{pk'}^* \\
&= \sum_{k,k'=0}^{N-1} C_{kk'} \exp\left(i\frac{2\pi}{N} p(k-k') \right) \\
&= \sum_{l=-(N-1)}^{N-1} (N - |l|) C_l \exp\left(-i\frac{2\pi}{N} pl \right) \\
&\approx N \sum_{l=-(N-1)}^{N-1} C_l \exp\left(-i\frac{2\pi}{N} pl \right). \qquad (A7)
\end{aligned}
$$

This is the statement of the Wiener-Khinchin theorem.

As an illustration of the Wiener-Khinchin theorem, consider a white-noise process for which $C_l^{\text{WN}} = \sigma^2 \delta_{l,0}$. Then Eq. (A7) yields PSD $\tilde{C}_p^{\text{WN}} = N\sigma^2$ regardless of the DFT frequency. This white-noise relation can be also derived directly:

$$
\begin{aligned}
\tilde{C}_p^{\text{WN}} &= \langle |\tilde{x}_p|^2 \rangle = N \sum_k \sum_{k'} U_{pk} C_{kk'}^{\text{WN}} U_{pk'}^* \\
&= N\sigma^2 \sum_k \sum_{k'} U_{pk} \delta_{kk'} U_{pk'}^* = N\sigma^2 \underbrace{(\mathbf{U}\mathbf{U}^\dagger)}_{=\mathbf{I}}{}_{pp} = N\sigma^2.
\end{aligned}
$$

We will need another property of PSDs: $\tilde{C}_p = \tilde{C}_{N-p}$. This relation immediately follows from Eq. (A4).

2. Probability distribution in frequency space for the deterministic signal

The derivation in this section essentially follows Ref. [34]. It corrects errors in that work related to the dc component and, in addition, includes the contribution from the Nyquist frequency.

Consider a data time series **d**, which can contain both the sought signal **s** and noise **n**: $d_k = s_k + n_k$, $k = \overline{0, N-1}$. The signal is prescribed by some model M. We assume that the noise is Gaussian with $\langle n_k \rangle = 0$, but not necessarily white. Then the likelihood is given by the multivariate Gaussian distribution for residuals $\boldsymbol{n} = \boldsymbol{d} - \boldsymbol{s}$,

$$p(\boldsymbol{d}|M,I) = \frac{1}{\sqrt{\det(2\pi \boldsymbol{C})}} \exp\left(-\frac{1}{2}\boldsymbol{n}^\dagger \boldsymbol{C}^{-1}\boldsymbol{n} \right), \quad (A8)$$

where I stands for the prior information proposition and the autocorrelation matrix has elements $C_{kk'} = \langle n_k n_{k'} \rangle$. Now we rotate the argument of the exponential to the DFT basis by inserting the identity $\mathbf{U}^\dagger\mathbf{U} = \mathbf{I}$: $\boldsymbol{n}^\dagger \boldsymbol{C}^{-1}\boldsymbol{n} = \boldsymbol{n}^\dagger(\mathbf{U}^\dagger\mathbf{U})\boldsymbol{C}^{-1}(\mathbf{U}^\dagger\mathbf{U})\boldsymbol{n} = (\mathbf{U}\boldsymbol{n})^\dagger(\mathbf{U}\boldsymbol{C}\mathbf{U}^\dagger)^{-1}(\mathbf{U}\boldsymbol{n})$. The indicated groups can be expressed in terms of DFT quantities $\mathbf{U}\boldsymbol{n} = \tilde{\boldsymbol{n}}/\sqrt{N}$ and $\mathbf{U}\mathbf{C}\mathbf{U}^\dagger = N^{-1}\tilde{\mathbf{C}}$ [see Eqs. (A2) and (A5)]. Further, we use the fact that the PSD matrix is diagonal, $\tilde{\mathbf{C}} = \text{diag}(\tilde{C}_p)$, to invert the matrix: $\tilde{\mathbf{C}}^{-1} = \text{diag}(\tilde{C}_p^{-1})$. Thus, the argument of the exponential is transformed into

$$-\frac{1}{2}\boldsymbol{n}^\dagger \boldsymbol{C}^{-1}\boldsymbol{n} = -\frac{1}{2}\sum_{p=0}^{N-1} \frac{|\tilde{n}_p|^2}{\tilde{C}_p}, \qquad (A9)$$

leading to the likelihood (we will recover the normalization factor below)

$$p_{\text{det}}(\tilde{\boldsymbol{d}}|M,I) \propto \prod_{p=0}^{N-1} \exp\left(-\frac{1}{2}\frac{|\tilde{n}_p|^2}{\tilde{C}_p} \right). \qquad (A10)$$

Here we used the label det to emphasize the deterministic (as opposed to stochastic) nature of the signal. Apparently, the spectral contributions become uncorrelated as a result of the basis rotation. As the data are real valued, we further use the redundancies $|\tilde{n}_{N-p}|^2 = |\tilde{n}_p|^2$ and $\tilde{C}_{N-p} = \tilde{C}_p$ and combine identical spectral contributions (notice that the $p = 0$ and $p = N/2$ contributions are treated as special cases as they do not have matching quantities)

$$
\begin{aligned}
p_{\text{det}}(\tilde{\boldsymbol{d}}|M,I) &\propto \exp\left[-\frac{1}{2}\left(\frac{|\tilde{n}_0|^2}{\tilde{C}_0} + \frac{|\tilde{n}_{N/2}|^2}{\tilde{C}_{N/2}} \right) \right] \\
&\times \prod_{p=1}^{N/2-1} \exp\left(-\frac{|\tilde{n}_p|^2}{\tilde{C}_p} \right). \qquad (A11)
\end{aligned}
$$

The volume element associated with this probability distribution reads

$$d\,\text{Re}(\tilde{n}_0)\,d\,\text{Re}(\tilde{n}_{N/2}) \prod_{p=1}^{N/2-1} d\,\text{Re}(\tilde{n}_p)\,d\,\text{Im}(\tilde{n}_p), \qquad (A12)$$

where we took into account that the dc and the Nyquist values are strictly real. The total number of random DFT variables is N and it remains equal to the number of sampled data points. To recover the normalization factor we can compute the Jacobian J of the transformation so that $p(\tilde{D}|M,I) = J \times p(D|M,I)$. Alternatively, as the transformation $\mathbf{U}$ is linear, we can simply normalize the distribution. With $\int_{-\infty}^{+\infty} \exp[-\frac{1}{2}x^2/\rho^2]dx = \sqrt{2\pi}\rho$ and $\int_{-\infty}^{+\infty} \exp[-(x^2+y^2)/\rho^2]dx\,dy = \pi\rho$, we arrive at the frequency-domain likelihood

$$p_{\text{det}}(\tilde{\boldsymbol{d}}|M,I) = \prod_{p=0}^{N/2} \frac{1}{(\beta_p^{-1}\pi \tilde{C}_p)^{\beta_p}} e^{-\beta_p |\tilde{n}_p|^2/\tilde{C}_p}. \qquad (A13)$$

Here $\beta_j = 1$ except for the dc and the Nyquist components for which $\beta_0 = \beta_{N/2} = 1/2$. It is worth emphasizing that we

treated the sought signal **s** as deterministic. In the above likelihood $\tilde{n}_p \equiv \tilde{d}_p - \tilde{s}_p$.

While we derived the DFT likelihood (A13) rigorously, this result is expected on qualitative grounds as the DFT components $\tilde{n}_p$ are sums of Gaussian random variables n_k, meaning that $\tilde{n}_p$ is also Gaussian distributed. Moreover, the DFT values are uncorrelated; thereby the DFT likelihood (A13) is a product of individual Gaussians.

3. Stochastic signal probability distribution and its likelihood in frequency space

Now let us assume that the sought signal **s** itself is stochastic and Gaussian distributed, with the mean value being zero. Then its probability distribution [cf. Eq. (A13)] reads

$$p(\tilde{\boldsymbol{s}}|M,I) = \prod_{p=0}^{N/2} \frac{1}{(\beta_p^{-1}\pi\,\tilde{S}_p)^{\beta_p}} \exp\left(-\beta_p \frac{|\tilde{s}_p|^2}{\tilde{S}_p}\right), \quad \text{(A14)}$$

where the signal PSD $\tilde{S}_p = \langle|\tilde{s}_p|^2\rangle$. At the same time for a specific realization of the signal, the likelihood is given by Eq. (A13),

$$p(\tilde{\boldsymbol{d}}|\tilde{S},I) = \prod_{p=0}^{N/2} \frac{1}{(\beta_p^{-1}\pi\tilde{C}_p)^{\beta_p}} e^{-\beta_p|\tilde{d}_p - \tilde{s}_p|^2/\tilde{C}_p}, \quad \text{(A15)}$$

where $\tilde{C}_p = \langle|\tilde{n}_p|^2\rangle$ is the noise PSD. Then the likelihood for a stochastic signal is obtained by marginalizing over realizations of the signal

$$p_{\text{stoch}}(\tilde{\boldsymbol{d}}|M,I) = \int d\tilde{s}\, p(\tilde{\boldsymbol{d}}|\tilde{S},I)p(\tilde{\boldsymbol{s}}|M,I). \quad \text{(A16)}$$

The integration can be carried out using explicitly, leading to

$$p_{\text{stoch}}(\tilde{\boldsymbol{d}}|M,I) = \prod_{p=0}^{N/2} \frac{1}{(\beta_p^{-1}\pi\,\tilde{\Sigma}_p)^{\beta_p}} e^{-\beta_p|\tilde{d}_p|^2/\tilde{\Sigma}_p}, \quad \text{(A17)}$$

with $\tilde{\Sigma}_p = \tilde{C}_p + \tilde{S}_p$. This result can also be understood without explicit marginalization: Consider a random variable $\tilde{\eta}_p \equiv \tilde{s}_p + \tilde{n}_p = \tilde{d}_p$. Because both $\tilde{s}_p$ and $\tilde{n}_p$ are Gaussian, their sum $\tilde{\eta}_p$ is Gaussian as well and it is distributed according to Eq. (A13). The associated PSD is

$$\langle|\tilde{\eta}_p|^2\rangle = \langle(\tilde{s}_p + \tilde{n}_p)(\tilde{s}_p + \tilde{n}_p)^*\rangle$$
$$= \langle|\tilde{s}_p|^2\rangle + 2\,\text{Re}\underbrace{\langle\tilde{s}_p\tilde{n}_p^*\rangle}_{=0} + \langle|\tilde{n}_p|^2\rangle = \tilde{C}_p + \tilde{S}_p = \tilde{\Sigma}_p.$$

Then the application of Eq. (A13) with $\tilde{n}_p \to \tilde{\eta}_p = \tilde{d}_p$ and $\tilde{C}_p \to \tilde{\Sigma}_p$ immediately yields Eq. (A17).

4. Likelihoods for a network

This section generalizes frequency-space likelihoods for deterministic and stochastic signals to a network of devices.

We consider a network of N_d devices. The network nodes can be degenerate and contain one or several devices. We will label the devices with letters at the beginning of the alphabet $a, b, \ldots$ and use superscripts for device labels and subscripts for time stamps. Then the time series $\{x_k^a\}$ refers to the time series of Sec. A 1 for the ath device. Each

device data time series $\{d_k^a\}$ can contain the noise component $\{n_k^a\}$, $\langle n_k^a\rangle = 0$. To streamline the notation, we introduce supervectors spanning the entire network time series: $\underline{x} = ((x_1^1, x_2^1, \ldots, x_N^1), \ldots, (x_1^{N_d}, x_2^{N_d}, \ldots, x_N^{N_d}))^T$. Supermatrices $\underline{C}$ are defined in a similar fashion. We will use underlined quantities to emphasize the use of this supervector space.

The correlation matrix $\underline{C}$ for a network is defined as a matrix with elements $\underline{C}_{kk'}^{ab} \equiv \langle n_k^a n_{k'}^b\rangle$. If devices are uncorrelated, $\underline{C}_{kk'}^{ab} \equiv \delta_{ab}\langle n_k^a n_{k'}^a\rangle$. We will however consider the general case, when the devices may share some noise channel, introduced, for example, by the device comparison techniques such as the use of an internode optical fiber. The PSD matrix $\underline{\tilde{C}}$ is generalized to have elements $\underline{\tilde{C}}_{pp'}^{ab} \equiv \langle\tilde{n}_p^a(\tilde{n}_{p'}^b)^*\rangle$.

First, consider a deterministic signal $\{s_k^a\}$ prescribed by a model M. We suppose each datum is composed of the noise and the sought signal: $d_k^a = s_k^a + n_k^a$. The time-domain likelihood is given by the multivariate Gaussian distribution

$$p(\underline{\boldsymbol{d}}|M,I) = \frac{1}{\sqrt{\det(2\pi\underline{C})}}\exp\left(-\frac{1}{2}\underline{\boldsymbol{n}}^\dagger\underline{C}^{-1}\underline{\boldsymbol{n}}\right), \quad \text{(A18)}$$

with I being prior information. Explicitly,

$$\underline{\boldsymbol{n}}^\dagger\underline{C}^{-1}\underline{\boldsymbol{n}} = \sum_{a,b=1}^{N_d}\sum_{k,k'=0}^{N-1} n_k^a(\underline{C}^{-1})_{kk'}^{ab}n_{k'}^b. \quad \text{(A19)}$$

Now we carry out the rotation to the DFT basis as in Sec. A 2. The relevant DFT supermatrix $\underline{U}$ is block diagonal and is composed of N_d DFT matrices U. Then

$$\underline{\boldsymbol{n}}^\dagger\underline{C}^{-1}\underline{\boldsymbol{n}} = \frac{1}{N}\underline{\tilde{\boldsymbol{n}}}^\dagger(\underline{U}\underline{C}\underline{U}^\dagger)^{-1}\underline{\tilde{\boldsymbol{n}}} = \underline{\tilde{\boldsymbol{n}}}^\dagger\underline{\tilde{C}}^{-1}\underline{\tilde{\boldsymbol{n}}}. \quad \text{(A20)}$$

Here the DFT supervectors are $\underline{\tilde{\boldsymbol{n}}} = ((\tilde{n}_1^1, \tilde{n}_2^1, \ldots, \tilde{n}_N^1), \ldots (\tilde{n}_1^{N_d}, \tilde{n}_2^{N_d}, \ldots, \tilde{n}_N^{N_d}))^T$, where the lower indices enumerate DFT frequencies. To efficiently invert $\underline{\tilde{C}}$, we reshuffle the components of $\underline{\tilde{\boldsymbol{n}}}$ so that $\underline{\tilde{\boldsymbol{n}}}' = ((\tilde{n}_1^1, \tilde{n}_1^2, \ldots, \tilde{n}_1^{N_D}), \ldots (\tilde{n}_N^1, \tilde{n}_N^2, \ldots, \tilde{n}_N^{N_d}))^T$, i.e., each subgroup shares the same DFT frequency. Then the reshuffled PSD matrix is block diagonal, each block $\underline{\tilde{C}}_p$ corresponding to a given DFT frequency: $(\underline{\tilde{C}}_p)^{ab} = \langle\tilde{n}_p^a(\tilde{n}_p^b)^*\rangle$. Indeed, for a stationary stochastic process, the network PSD is diagonal in frequency indices for reasons discussed in Sec. A 1: $\underline{\tilde{C}}_{pp'}^{ab} \equiv \delta_{pp'}\langle\tilde{n}_p^a(\tilde{n}_p^b)^*\rangle$. The reshuffling is useful because an inverse of a block-diagonal matrix is itself a block-diagonal matrix, with submatrices $\underline{\tilde{C}}_p^{-1}$.

The resulting frequency-domain network likelihood for a deterministic signal

$$p_{\text{det}}(\underline{\tilde{\boldsymbol{d}}}|M,I) = \prod_{p=0}^{N/2} \frac{1}{[\beta_p^{-1}\pi\,\det(\underline{\tilde{C}}_p)]^{\beta_p}}$$
$$\times \exp[-\beta_p(\underline{\tilde{\boldsymbol{d}}}_p - \underline{\tilde{\boldsymbol{s}}}_p)^\dagger\underline{\tilde{C}}_p^{-1}(\underline{\tilde{\boldsymbol{d}}}_p - \underline{\tilde{\boldsymbol{s}}}_p)], \text{(A21)}$$

where data vectors $\underline{\tilde{\boldsymbol{d}}}_p \equiv (\tilde{d}_p^1, \tilde{d}_p^2, \ldots, \tilde{d}_p^{N_D})$, signal vectors $\underline{\tilde{\boldsymbol{s}}}_p \equiv (\tilde{s}_p^1, \tilde{s}_p^2, \ldots, \tilde{s}_p^{N_D})$, and PSDs $(\underline{\tilde{C}}_p)^{ab} = \langle\tilde{n}_p^a(\tilde{n}_p^b)^*\rangle$. As in Eq. (A13), $\beta_p = 1$ except for the dc and the Nyquist components for which $\beta_0 = \beta_{N/2} = 1/2$.

Following the steps of Sec. A 3, we generalize Eq. (A21) to stochastic signals

$$p_{\text{stoch}}(\underline{\tilde{d}}|M,I) = \prod_{p=0}^{N/2} \frac{1}{\left[\beta_p^{-1}\pi \det(\underline{\tilde{\Sigma}}_p)\right]^{\beta_p}} e^{-\beta_p \underline{\tilde{d}}_p^\dagger \underline{\tilde{\Sigma}}_p^{-1} \underline{\tilde{d}}_p}, \quad \text{(A22)}$$

with $\underline{\tilde{\Sigma}}_p = \underline{\tilde{C}}_p + \underline{\tilde{S}}_p$. The elements of the signal PSD matrix are $(\underline{\tilde{S}}_p)^{ab} = \langle \tilde{s}_p^a (\tilde{s}_p^b)^* \rangle$. This result can be obtained immediately following the arguments given just below Eq. (A17). Alternatively, one could explicitly carry out marginalization over signal values. In this case, the marginalization can be aided by the convolution formula of two multivariate Gaussian distributions

$$\int \frac{e^{-(x-y)^T A^{-1}(x-y)/2}}{\sqrt{\det(2\pi A)}} \frac{e^{-y^T B^{-1} y/2}}{\sqrt{\det(2\pi B)}} dy = \frac{e^{-x^T(A+B)^{-1}x/2}}{\sqrt{\det[2\pi(A+B)]}}. \quad \text{(A23)}$$

A more general convolution formula can be found in [44]. Equations (A21) and (A22) correct corresponding equations in Ref. [44] for the dc and Nyquist contributions.

APPENDIX B: ESTIMATORS OF THE MEAN AND VARIANCE OF THE COUPLING STRENGTH [EQS. (13) AND (14)]

Here I derive the maximum-likelihood estimators of the mean and variance of the coupling strength for stochastic signal. In the main text, the noise PSD was defined as $\tilde{\rho}_p = \langle |\tilde{n}_p|^2 \rangle$ and the dark-matter signal PSD as $\langle |\tilde{s}_p|^2 \rangle = A^2 \gamma_X^2 \langle |\tilde{\phi}_p|^2 \rangle$, where γ_X is the coupling strength to dark matter and A is the (fixed) device constant. We will use the parametrization $\langle |\tilde{s}_p|^2 \rangle = \Gamma \tilde{S}_p$, with $\Gamma \equiv (\gamma_X)^2$ and $\tilde{S}_p \equiv A^2 \langle |\tilde{\phi}_p|^2 \rangle$.

The likelihood is given by Eq. (A17). For simplicity, we assume that the dc component has been removed from the data and the Nyquist component was filtered out. Then

$$p_{\text{stoch}}(\tilde{d}|\Gamma,I) = \prod_{p=1}^{N/2-1} \frac{1}{\pi(\tilde{\rho}_p + \Gamma\tilde{S}_p)} e^{-|\tilde{d}_p|^2/(\tilde{\rho}_p + \Gamma\tilde{S}_p)}. \quad \text{(B1)}$$

We would like to determine the posterior distribution $p(\Gamma|\tilde{d},I)$ for the parameter Γ given data $\tilde{d}$ and prior information I. To this end we invoke the Bayes theorem

$$p(\tilde{d},\Gamma|I) = p(\tilde{d}|I)p(\Gamma|\tilde{d},I) = p(\Gamma|I)p(\tilde{d}|\Gamma,I),$$

leading to

$$p(\Gamma|\tilde{d},I) = \frac{p(\Gamma|I)}{p(\tilde{d}|I)} p_{\text{stoch}}(\tilde{d}|\Gamma,I). \quad \text{(B2)}$$

Here $p(\Gamma|I)$ gives the prior probability density for the parameter Γ. We assume that there is no prior knowledge about the value of the parameter. For example, we could take $p(\Gamma|I)$ to be a uniform distribution in the range $[0,\Gamma_{\max}]$, where $\Gamma_{\max}$ is sufficiently large. Here $p(\tilde{d}|I)$ is a normalization constant.

Now we put the posterior distribution $p(\Gamma|\tilde{d},I)$ into a Gaussian form (strictly speaking, we are using the Laplace approximation)

$$p(\Gamma|\tilde{d},I) \approx \mathcal{C} \exp\left(-\frac{(\Gamma-\hat{\Gamma})^2}{2(\hat{\sigma}_\Gamma)^2}\right), \quad 0 < \Gamma < \Gamma_{\max}, \quad \text{(B3)}$$

where $\hat{\Gamma}$ and $\hat{\sigma}_\Gamma$ are the maximum-likelihood estimators for the mean and the standard deviation and are to be determined. The proportionality factor $\mathcal{C}$ does not depend on Γ. The probability maximum is reached at $\Gamma = \hat{\Gamma}$. Consider an auxiliary construction

$$\ln[p(\Gamma|\tilde{d},I)] \approx \ln\mathcal{C} - \frac{(\Gamma-\hat{\Gamma})^2}{2(\hat{\sigma}_\Gamma)^2}. \quad \text{(B4)}$$

Then the estimator values can be determined from

$$\left[\frac{d}{d\Gamma}\ln[p(\Gamma|\tilde{d},I)]\right]_{\Gamma=\hat{\Gamma}} = 0, \quad \text{(B5)}$$

$$\frac{1}{(\hat{\sigma}_\Gamma)^2} = -\left[\frac{d^2}{d^2\Gamma}\ln[p(\Gamma|\tilde{d},I)]\right]_{\Gamma=\hat{\Gamma}}, \quad \text{(B6)}$$

where $p(\Gamma|\tilde{d},I)$ is to be replaced with $p_{\text{stoch}}(\tilde{d}|\Gamma,I)$ [Eq. (A17)]. Evaluating the derivatives and linearizing the resulting expressions for weak signals $\Gamma\tilde{S}_p \ll \tilde{\rho}_p$, we arrive at

$$\frac{1}{(\hat{\sigma}_\Gamma)^2} = \sum_{p=1}^{N/2-1} (2|\tilde{d}_p|^2/\tilde{\rho}_p - 1)\left(\frac{\tilde{S}_p}{\tilde{\rho}_p}\right)^2, \quad \text{(B7)}$$

$$\hat{\Gamma} = (\hat{\sigma}_\Gamma)^2 \sum_{p=1}^{N/2-1} (|\tilde{d}_p|^2/\tilde{\rho}_p - 1)\frac{\tilde{S}_p}{\tilde{\rho}_p}. \quad \text{(B8)}$$

With $\hat{\gamma}_X = \sqrt{\hat{\Gamma}}$ and $\hat{\sigma}_{\gamma_X} = \sqrt{\hat{\sigma}_\Gamma}$, these equations lead to Eqs. (13) and (14).

APPENDIX C: DERIVATION OF EQ. (16)

We start with the estimate for the standard deviation of the coupling strength

$$\sigma_{\gamma_X}^{(1)} \approx A^{-1}\left\{\sum_{p=1}^{N/2-1}\left(\frac{\langle|\tilde{\phi}_p|^2\rangle}{\tilde{\rho}_p}\right)^2\right\}^{-1/4}. \quad \text{(C1)}$$

For white noise $\tilde{\rho}_p = N\sigma^2$,

$$\sigma_{\gamma_X}^{(1)} \approx A^{-1}\sigma\left\{\frac{1}{N^2}\sum_{p=1}^{N/2-1}\langle|\tilde{\phi}_p|^2\rangle^2\right\}^{-1/4}. \quad \text{(C2)}$$

Further, we use the relationship of the discretized field PSD to the dark-matter line shape

$$\langle|\tilde{\phi}_p|^2\rangle = \frac{\pi N}{\Delta_t}\Phi_0^2 F(\omega_p), \quad \text{(C3)}$$

leading to

$$\sigma_{\gamma_X}^{(1)} \approx A^{-1}\sigma\left\{\frac{1}{N^2}\sum_{p=1}^{N/2-1}\frac{\pi^2 N^2}{\Delta_t^2}\Phi_0^4[F(\omega_p)]^2\right\}^{-1/4}$$

$$= (A\Phi_0)^{-1}\sigma\left\{\frac{\pi^2}{\Delta_t^2}\sum_{p=1}^{N/2-1}[F(\omega_p)]^2\right\}^{-1/4}. \quad \text{(C4)}$$

Now we can convert the sum to an integral by introducing the DFT frequency step $\Delta_\omega = \frac{2\pi}{N\Delta_t}$:

$$\sigma_{\gamma_X}^{(1)} = (A\Phi_0)^{-1}\sigma\left\{\frac{\pi N}{2\Delta_t}\sum_{p=1}^{N/2-1}\Delta_\omega[F(\omega_p)]^2\right\}^{-1/4} = (A\Phi_0)^{-1}\sigma\left\{\frac{\pi^2}{\Delta_t}\frac{N}{2\pi}\int_0^\infty d\omega[F(\omega_p)]^2\right\}^{-1/4}. \tag{C5}$$

For the fiducial value of $\eta = 1$,

$$\int_0^\infty d\omega[F(\omega_p)]^2 = \tau_c^2\frac{1}{2\pi e^2}\int_{\omega_\phi'-(2\tau_c)^{-1}}^\infty e^{-2(\omega-\omega_\phi')\tau_c}\sinh^2[\sqrt{1+2(\omega-\omega_\phi')\tau_c}] = \tau_c\frac{1}{4\pi e^2}\int_{-1}^\infty e^{-x}\sinh^2(\sqrt{1+x}) = \frac{\mathrm{erf}(1)}{8\sqrt{\pi}}\tau_c.$$

Thus,

$$\sigma_{\gamma_X}^{(1)} = (A\Phi_0)^{-1}\sigma\left\{\frac{\sqrt{\pi}\,\mathrm{erf}(1)}{16}\right\}^{-1/4}\left\{N\left(\frac{\tau_c}{\Delta_t}\right)\right\}^{-1/4} \approx 2.4\left(\frac{\Delta_t}{N\tau_c}\right)^{1/4}\frac{\sigma}{A\Phi_0}, \tag{C6}$$

which is Eq. (16).

[1] J. L. Feng, Annu. Rev. Astron. Astrophys. **48**, 495 (2010).

[2] G. Bertone, D. Hooper, and J. Silk, Phys. Rep. **405**, 279 (2005).

[3] M. S. Safronova, D. Budker, D. DeMille, D. F. J. Kimball, A. Derevianko, and C. W. Clark, arXiv:1710.01833.

[4] A. Arvanitaki, J. Huang, and K. Van Tilburg, Phys. Rev. D **91**, 015015 (2015).

[5] P. W. Graham, D. E. Kaplan, J. Mardon, S. Rajendran, and W. A. Terrano, Phys. Rev. D **93**, 075029 (2016).

[6] A. A. Geraci and A. Derevianko, Phys. Rev. Lett. **117**, 261301 (2016).

[7] D. Budker, P. W. Graham, M. Ledbetter, S. Rajendran, and A. O. Sushkov, Phys. Rev. X **4**, 021030 (2014).

[8] Y. V. Stadnik and V. V. Flambaum, Phys. Rev. Lett. **114**, 161301 (2015).

[9] Y. V. Stadnik and V. V. Flambaum, Phys. Rev. A **93**, 063630 (2016).

[10] A. Arvanitaki, S. Dimopoulos, and K. Van Tilburg, Phys. Rev. Lett. **116**, 031102 (2016).

[11] A. Arvanitaki, P. W. Graham, J. M. Hogan, S. Rajendran, and K. Van Tilburg, arXiv:1606.04541.

[12] D. Budker and A. Derevianko, Phys. Today **68**(9), 10 (2015).

[13] M. Pospelov, S. Pustelny, M. P. Ledbetter, D. F. Jackson Kimball, W. Gawlik, and D. Budker, Phys. Rev. Lett. **110**, 21803 (2013).

[14] A. Derevianko and M. Pospelov, Nat. Phys. **10**, 933 (2014).

[15] J. Magaña, T. Matos, V. Robles, and A. Suárez, J. Phys.: Conf. Ser. **378**, 012012 (2012).

[16] R. Essig, J. J. A. Jaros, W. Wester *et al.*, Dark sectors and new, light, weakly-coupled particles, arXiv:1311.0029.

[17] P. W. Graham, I. G. Irastorza, S. K. Lamoreaux, A. Lindner, and K. A. van Bibber, Annu. Rev. Nucl. Part. Sci. **65**, 485 (2015).

[18] M. Pospelov, A. Ritz, and M. Voloshin, Phys. Rev. D **78**, 115012 (2008).

[19] S. Dimopoulos and G. F. Giudice, Phys. Lett. B **379**, 105 (1996).

[20] N. Arkani-Hamed, L. Hall, D. Smith, and N. Weiner, Phys. Rev. D **62**, 105002 (2000).

[21] C. P. Burgess, A. Maharana, and F. Quevedo, J. High Energy Phys. 05 (2011) 10.

[22] M. Cicoli, C. P. Burgess, and F. Quevedo, J. High Energy Phys. 10 (2011) 119.

[23] T. R. Taylor and G. Veneziano, Phys. Lett. B **213**, 450 (1988).

[24] T. Damour and A. M. Polyakov, Nucl. Phys. B **423**, 532 (1994).

[25] M. Kuhlen, A. Pillepich, J. Guedes, and P. Madau, Astrophys. J. **784**, 161 (2014).

[26] K. Freese, M. Lisanti, and C. Savage, Rev. Mod. Phys. **85**, 1561 (2013).

[27] M. Vogelsberger, A. Helmi, V. Springel, S. D. M. White, J. Wang, C. S. Frenk, A. Jenkins, A. Ludlow, and J. F. Navarro, Mon. Not. R. Astron. Soc. **395**, 797 (2009).

[28] R. Catena and P. Ullio, J. Cosmol. Astropart. Phys. 08 (2010) 004.

[29] J. A. Peacock, *Cosmological Physics* (Cambridge University Press, Cambridge, 1999), Sec. 16.3 .

[30] S. Weinberg, *Cosmology* (Oxford University Press, New York, 2008).

[31] S. Pustelny, D. F. Jackson Kimball, C. Pankow, M. P. Ledbetter, P. Wlodarczyk, P. Wcislo, M. Pospelov, J. R. Smith, J. Read, W. Gawlik, and D. Budker, Ann. Phys. (Berlin) **525**, 659 (2013).

[32] B. M. Roberts, G. Blewitt, C. Dailey, M. Murphy, M. Pospelov, A. Rollings, J. Sherman, W. Williams, and A. Derevianko, Nat. Commun. **8**, 1195 (2017).

[33] S. Vitale, Gen. Relativ. Gravit. **46**, 1730 (2014).

[34] J. D. Romano and N. J. Cornish, Living Rev. Relativ. **20**, 1 (2017).

[35] W. von der Linden, V. Dose, and U. von Toussaint, *Bayesian Probability Theory: Applications in the Physical Sciences* (Cambridge University Press, New York, 2014), Sec. 23 .

[36] P. Wcisło, P. Morzyński, M. Bober, A. Cygan, D. Lisak, R. Ciuryło, and M. Zawada, Nat. Astron. **1**, 0009 (2016).

[37] K. Van Tilburg, N. Leefer, L. Bougas, and D. Budker, Phys. Rev. Lett. **115**, 011802 (2015).

[38] A. Hees, J. Guéna, M. Abgrall, S. Bize, and P. Wolf, Phys. Rev. Lett. **117**, 061301 (2016).

[39] A. Derevianko and H. Katori, Rev. Mod. Phys. **83**, 331 (2011).

[40] W. Zhang, J. M. Robinson, L. Sonderhouse, E. Oelker, C. Benko, J. L. Hall, T. Legero, D. G. Matei, F. Riehle, U. Sterr, and J. Ye, Phys. Rev. Lett. **119**, 243601 (2017).

[41] C. Lisdat *et al.*, Nat. Commun. **7**, 12443 (2016).

[42] F. Riehle, Nat. Photon. **11**, 25 (2017).

[43] P. Gregory, *Bayesian Logical Data Analysis for the Physical Sciences: A Comparative Approach with Mathematica Support* (Cambridge University Press, Cambridge, 2010).

[44] N. J. Cornish and J. D. Romano, Phys. Rev. D **87**, 122003 (2013).